Supplementary Information (SI) for Materials Horizons.

Supporting Information

Dirac-Cone induced Metallic Conductivity in $Cu_3(HHTP)_2$: High-Quality MOF Thin Films Fabricated via ML-Driven Robotic Synthesis

Chatrawee Scheiger [a, +], Jonas F. Pöhls [b, +], Mersad Mostaghimi [c], Lena Pilz [a], Mariana Kozlowska [c,], Yidong Liu [a], Lars Heinke [d], Carlos Cesar Bof Bufon [e], R. Thomas Weitz [b,f], Wolfgang Wenzel [c,*], and Christof Wöll [a,*]

[a] Institute of Functional Interfaces, Karlsruhe Institute of Technology, Hermann-von-Helmholtz-Platz 1, 76344 Eggenstein-Leopoldshafen, Germany

[b] I. Institute of Physics, Georg-August-University Göttingen, Friedrich-Hund-Platz 1, 37077 Göttingen

[c] Institute of Nanotechnology, Karlsruhe Institute of Technology, Hermann-von-Helmholtz-Platz 1, 76344 Eggenstein-Leopoldshafen, Germany

[d] Institute of Chemistry and Biochemistry, Freie Universität Berlin, Arnimallee 22, 14915 Berlin

[e] Institute of Geosciences and Exact Sciences, Department of Physics, São Paulo State University (UNESP), Rio Claro, SP, Brazil

[f] International Center for Advanced Studies of Energy Conversion (ICASEC), University of Göttingen, Germany

[+]Equal contribution

* Corresponding authors: wolfgang.wenzel@kit.edu, christof.woell@kit.edu

1. Experimental

1.1 Materials

The silicon wafers were purchased from Siegert Wafer. The thickness of the silicon wafer is 525 µm with a resistivity of 1-5 Ω cm^{-1}.

All chemicals are commercial products and were employed without further purification. Copper (II) acetate monohydrate was purchased from Merck. 2,3,6,7,10,11-Hexahydroxytriphenylene (HHTP) was purchased from ACROS. Ethanol (AR grade, ≥99.8%) was purchased from AnalaR NORMAPUR.

1.2 Fabrication of SURMOFs

1.2.1 Substrate

The silicon wafers were initially subjected to thermal activation at 1000°C for 1 h to enhance hydrophilicity on the surface, resulting in a light-blue silicon wafer. Subsequently, the activated silicon wafers with dimensions of 2 cm × 3 cm were used as substrates. All substrates were treated with oxygen plasma for 30 min immediately before use.

1.2.2 Synthesis procedure

The synthesis of Cu_3HHTP_2 SURMOF was conducted using an industrial six-axis dipping robot from Stäubli in a nitrogen-filled glove box. Following the plasma treatment, three substrates were mounted on the sample holder and sequentially immersed in various solutions of the metal salts, organic linker, and rinsing solution. The solution volumes were set at 210 mL to match the container size of the dipping robot. In adherence to synthesis conditions, a mixture of water and ethanol was used as a solvent for the organic linker and rinsing solution, whereas pure ethanol served as a solvent for the metal salt. Ultrasonication was applied to ensure homogenous mixing of the solutions. The respective amounts of substances are provided in Table S1.

The growth of the Cu_3HHTP_2 SURMOF occurred in a layer-by-layer fashion through a cycle consisting of: 1) metal solution (10 min); 2) rinsing (5min); 3) additional rinsing in the ultrasonic bath (given time following to SyCoFinder); 4) linker solution (15 min); 5) rinsing (5min); 6) additional rinsing in the ultrasonic bath (given time following to SyCoFinder). The Cu_3HHTP_2 film was grown for 40 cycles under all synthesis conditions. The studied parameters and their corresponding ranges, defined based on our previous study, are demonstrated in Table S1. Detailed information regarding the precise amounts of all variables for each synthesis condition, as well as the setup of the dipping robot, is provided below.

1.3 Machine learning approach

To account for the full range of potential structural effects and to optimize thin film quality within the machine learning framework, four objectives were incorporated into the fitness function. These objectives were derived from out-of-plane XRD, in-plane XRD, and UV-Vis measurements for each synthesis condition proposed by SyCoFinder.

Among these four objectives, one served as an exclusion criterion: to evaluate the phase identity measured XRD signals were compared to simulated ones, and non-matching results were discarded from further characterization. The remaining three objectives were: (1) crystallinity of both out-of-plane and in-plane XRD curves, (2) I.Breadth, which targets domain size in the thin film, and (3) UV-Vis absorption, which provides insight into electronic properties.

Each objective, except for the exclusion criterion, was assigned a fitness value between zero and one. These values were then multiplied to determine the total fitness score for a given experiment. This feedback mechanism guided the machine learning algorithm in generating the next, progressively optimized iteration.

The computational aspect of the optimization process followed the steps outlined in the SyCoFinder web application. Initially, variable parameters and their ranges, as well as the number of experiments were defined. SyCoFinder accordingly generated a Diverse set using farthest point sampling (MaxMin method) based on the specified variable parameters and ranges. This resulted in the first set, or first generation, comprising ten distinct synthesis conditions. After the synthesis and characterization, the fitness values were examined. The identical synthesis conditions, along with their fitness values were fed back into the web application, generating a new set of ten synthesis conditions (second generation) for further synthesis, characterization, and ranking.

In this optimization process, a genetic algorithm (GA) was employed to generate new sets of experiments, starting from the second generation. The GA utilized genetic operations, including selection, crossover, and mutation, to produce offspring from the preceding generations. In this approach, two trials from the preceding generation were chosen as parents, and their synthesis variables, treated as genes, were merged through a crossover operation to create a novel synthesis trial as an offspring. To introduce an opportunity for exploration beyond the prior generations, certain genes were allowed to undergo mutation. This evolutionary process of generations was assigned as GA1 and GA2 before the results were deemed satisfying. For a more detailed of the machine learning method applied we refer the reader to Moosavi et al.[1]

In the final step, once the machine learning optimization is complete, SyCoFinder allows users to evaluate the significance of the selected variables on the optimization outcome. This step, called 'Importance of Variables,' employs a random forest-embedded method to assign relative values between zero and one to each chosen variable.

1.4 Fitness

The genetic algorithm, which generates a new population of parameters based on modification of the existing population, is guided by a fitness value ranging from 0 to 1. Higher fitness values in the synthesis conditions increase the likelihood of being selected as parents for the next generation. By utilizing a ranking-based selection algorithm, the fitness equations can easily be adapted to any multidimensional target. In this work, optimizations targeting crystallinity, crystal domain size, and metallic behaviors of the Cu_3HHTP_2 SURMOF in the farthest UV regime, which we believe to influence the electrical conductivity of the Cu_3HHTP_2 SURMOF, were incorporated into the fitness equation as follows:

$$\text{Fitness} = \text{fitness(phase identity)} \times \text{fitness(crystallinity)} \times \text{fitness(I.Breadth)} \times \text{fitness(absorption band)} \quad (1)$$

$$\text{Fitness(phase identity)} = \begin{cases} 1, if \dfrac{f_1 + f_2 + f_3}{3} = 1 \\ 0, else \end{cases} \quad (2)$$

Fitness (phase identity) was evaluated by comparing the positions of the measured XRD diffraction peaks of the samples to a calculated XRD diffractogram from a CIF file. The variable f_x represents the fitness (phase identity) of samples, with x having values of 1, 2, or 3, corresponding to the three samples from each synthesis condition. A match between the measured XRD pattern and the calculated XRD pattern assigns a value of 1 to f_x. Conversely, the absence of measured XRD peaks compared to the calculated XRD pattern, in one or all samples, results in a value of 0 for the f_x.

$$\text{Fitness(crystallinity)} = 0.5[\text{Norm.}(\frac{Re_1 + Re_2 + Re_3}{3})_{\text{in-plane}}] + 0.5[\text{Norm.}(\frac{Re_1 + Re_2 + Re_3}{3})_{\text{out-of-plane}}] \quad (3)$$

The reduced area (Re) represents the crystalline region computed from the XRD diffractogram of each sample, obtained under various synthesis conditions using the DIFFRAC.EVA software from Bruker. This assessment was performed on raw data without background subtraction. The average reduced area for each synthesis condition was then normalized to the maximum reduced area within the same generation. Both in-plane and out-of-plane XRD data were included in the calculation.

$$\text{Fitness(I.Breadth)} = \frac{\frac{1}{IB_X}}{IB_{Min}};\ \text{where } IB_x = \frac{I_{B1} + I_{B2} + IB_3}{3} \tag{4}$$

Breadth integral (I. Breadth) represents the peak width at 50% of the peak height intensity in the XRD diffractogram. According to Scherrer's equation, a smaller peak width indicates a larger crystal domain size, suggesting a reduction in grain boundaries that impede electron transfer within the film. Therefore, the average I.Breadth (IBx) from the three samples for each synthesis condition was normalized to the minimum I.Breadth within the same generation.

$$\text{Fitness (absorption band)} = \frac{A_x}{A_{Max}};\ \text{where } A_x = \frac{A_{x1} + A_{x2} + A_{x3}}{3} \tag{5}$$

The electronic properties of the Cu_3HHTP_2 SURMOF were investigated using the UV absorption band between 575 – 625 nm, suggesting metallic behaviors of the Cu_3HHTP_2 SURMOF. The integrated areas under the UV-Vis absorption band between 575 – 625 nm from three samples for each synthesis condition were averaged. This average value was then normalized to the maximum integrated area within the same generation.

Table S1. Optimized parameter sets obtained by the ML algorithm in SciCoFInder machine learning approach in descending fitness order

Fitness	[Metal] (mmol L^{-1})	[Linker] (mmol L^{-1})	Ultrasonication time (s)	water (mL)	Defect healing time (h)
0.79	1.66	0.30	31	19.23	48.71
0.76	1.20	0.20	24	21.70	50.00
0.57	4.55	0.29	40	16.80	33.75
0.53	1.42	0.30	46	18.28	26.27
0.48	5.10	0.24	65	22.61	17.69
0.47	4.25	0.12	44	19.64	41.83
0.47	1.20	0.13	24	18.22	35.17
0.40	5.04	0.10	94	18.68	24.60
0.40	5.29	0.25	62	19.69	47.25
0.37	5.62	0.30	38	18.90	50.00
0.36	5.94	0.18	24	17.96	34.16
0.36	7.30	0.30	100	21.70	50.00
0.34	7.30	0.10	24	21.70	32.00
0.34	1.20	0.30	62	21.70	14.00
0.31	4.25	0.30	24	16.80	50.00
0.28	7.30	0.10	62	16.80	50.00
0.28	7.30	0.20	100	16.80	14.00
0.25	1.20	0.10	24	16.80	14.00
0.23	4.25	0.10	100	21.70	14.00
0.17	1.20	0.10	100	19.25	50.00

2. Material characterization

2.1 X-ray diffraction (XRD)

Out-of-plane X-ray diffraction (XRD) measurements were conducted using a Bruker D8-Advance diffractometer equipped with a LynxEye position-sensitive detector in θ–θ geometry. The Cu_3HHTP_2 SURMOFs synthesized under various conditions were irradiated with Cu $K\alpha_{1,2}$ radiation ($\lambda = 0.154018$ nm). XRD diffractograms were recorded over a 2θ range from 25° to 31.5°, with a scan step of 0.02° and a scan time of 1 s per step, at 40 kV and 40 mA. To improve to diminish the signal-to-noise ratio, each sample was measured 10 times, and the resulting XRD diffractograms were accumulated using the DIFFRAC.EVA software version 5.2.0.3 from Bruker. All XRD patterns were executed with height error and background corrections using the same software. Additionally, the peaks between $2\theta = 67°$ to $2\theta = 72°$ were recorded to identify the characteristic diffraction peak of the silicon substrate, which served as a reference.

In-plane (non-co-planar orientation) XRD measurements were performed on a Bruker D8 Discover instrument, equipped with a quarter Eulerian cradle, tilt-stage, and 2.3° Soller-slits in θ–2θ geometry. XRD diffractograms were recorded from $2\theta = 3°$ to 30°, with a scan step of 0.02° and a scan time of 1 s per step at 40 kV and 35 mA using Cu $K\alpha_{1,2}$-radiation ($\lambda = 0.154018$ nm).

Crystallinity was assessed with an integrated routine from Bruker by comparing the measured diffractograms to a simulated powder diffractogram to validate phase identity.

2.2 UV-Vis spectroscopy

All UV-Vis absorption spectra were recorded by Agilent Cary 5000 UV–vis–NIR spectrophotometer in a range of 200 – 800 nm with a reflection mode.

2.3 Conductivity measurement

The electrical gold contacts (45 nm thickness) for the conductivity measurements on the µm-scale were evaporated in a solvent-free process through a shadow mask with a small evaporation rate of 0.5 Å/s in high vacuum. See Fig. S5 for an SEM image of a contacted film. The measured I-V curves show direction independent a classical ohmic behaviour indicating an ideal injection and the absence of barriers or junctions at the metal-MOF interface.

For the measurements on the nm-scale, contacts were prepared using electron-beam lithography. A PMMA resist (Anisol 950k 4,5%, Allresist) is applied in a spin coating process (30 s, 4000 1/s). The lithography was carried at a Raith EBL system, with a 7.5 µm aperture, 5 nm step size and a dose of 110 $\mu C/cm^2$ for the contacts and a 60 µm aperture, 60 nm step size and a dose of 170 $\mu C/cm^2$ for the corresponding contact pads. Development after patterning was performed in a 1:3 MIBK:IPS solution. The contacts were thermally evaporated in a UNIVEX chamber, with a adhesion layer of 1.5 nm Cr and 40 nm Au. Lift-off was carried out in aceton. The contact separation is 100 nm and the channel width is 40 µm.

The temperature dependent transport measurements as well as the room temperature measurements for the nm- and µm scale device were performed at a Lakeshore CRX-VF probe station at vacuum conditions with $p < 2 \times 10^{-7}$ mbar. For the contacts to the contact pads ZN50R-CVT-25-BECU flexible temperature probes were used, which are spring-loaded. The measurements were performed in a four-terminal configuration using a Keithley 2450 source meter, to exclude contact resistance. The measurements were performed with applied currents in the range of ± 10 µA to the outer two contacts while measuring the voltage drop at the inner contacts.

A temperature dependent measurement of the conductivity at the µm scale, see Fig. S4, the measurements of the nm spaced contacts are shown in the main manuscript.

The thicknesses of the films used for the conductivity measurements have been determined using tapping mode atomic force microscopy in a Jupiter AFM from Oxford Instruments. This resulted in 620 nm for the long-channel shadow mask sample and 650 nm for the short-channel electron beam lithography sample.

2.4 Scanning Electron Microscopy (SEM)

Morphologies and cross-section images of the Cu_3HHTP_2 SURMOF were investigated using a XL30 ESEM FEG (Environmental Scanning Electron Microscope XL30 Field Emission Gun, Philips) in high vacuum mode at 10 kV.

The thicknesses of the films used for the conductivity measurements have been determined using tapping mode atomic force microscopy in a Jupiter AFM from Oxford Instruments. This resulted in 620 nm for the long-channel shadow mask sample and 650 nm for the short-channel electron beam lithography sample.

Table S2. Previous reports on electrical conductivities of $Cu_3(HHTP)_2$

Measuring techniques	T (K)	Conductivity ($S\ m^{-1}$)	Ref.
Single crystal (4-probe)	295	150	[2]
Single crystal (2-probe)	295	50	
Single crystal (4-probe)	300	29	[3]
Film (4-probe)	100	300	this work
Film (4-probe)	RT	240	this work
Film (4-probe)	300	29	[4]
Film (2-probe)	300	11	[5]
Film (FET)	300	8.74	[6]
Film (4-probe)	RT	2.3	[7]
Film (2-probe)	RT	2	[8]
Film-40 (4-probe)	RT	0.228	[9]
Film-70 (4-probe)		4.86×10^{-2}	
Film (4-probe)	RT	10^{-2}	[10]
Pellet (4-probe)	RT	4.5	[7]
Pellet (2-probe)	-		[11]
Particle (air synthesis)		3	
Rod (air synthesis)		2	
Block		1	
Rod		0.4	
Flake		0.4	
Pellet (2-probe)	298	1	[12]
Electrode composite		4	
Pellet (4-probe)	RT	2	[13] [14]
Pellet (2-probe)	295	1.5	[15]

Pellet (4-probe)	RT	0.8	[16]
Pellet (4-probe)	-	0.76	[17] [18]
Pellet (2-probe)	-	0.7	[19]
Pellet (2-probe)	297	0.3	
Pellet (4-probe)	300	0.19	

Table S3. The studied parameters and their corresponding ranges for variation as chosen parameters

Parameter	Range
Metal concentration	1.2 – 7.3 mmol L^{-1}
Linker concentration	0.1 – 0.3 mmol L^{-1}
Ultrasonically-assisted cleaning time	24 – 100 s
Amount of water as a modulator	16.8 – 21.7 mL
Defect healing time	14 – 50 h

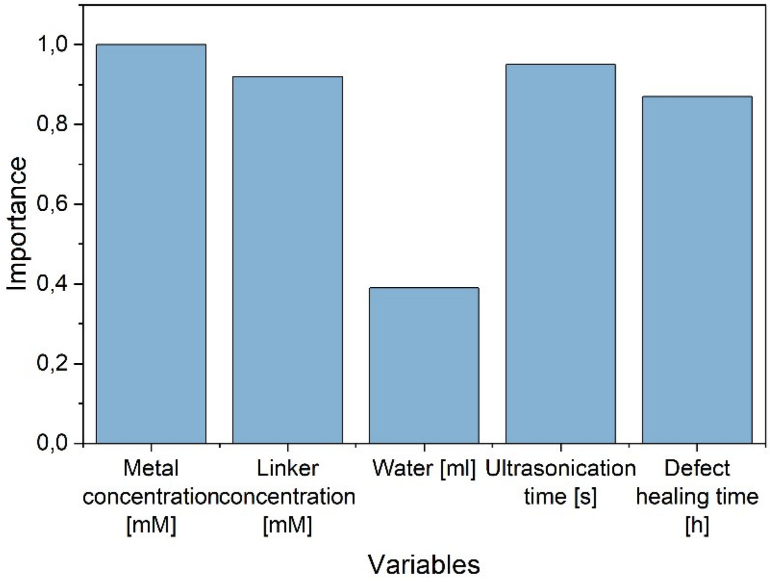

Figure S1. Relative importance of variables, revealing the influence of the chosen variables on the outcome of the machine learning optimization.

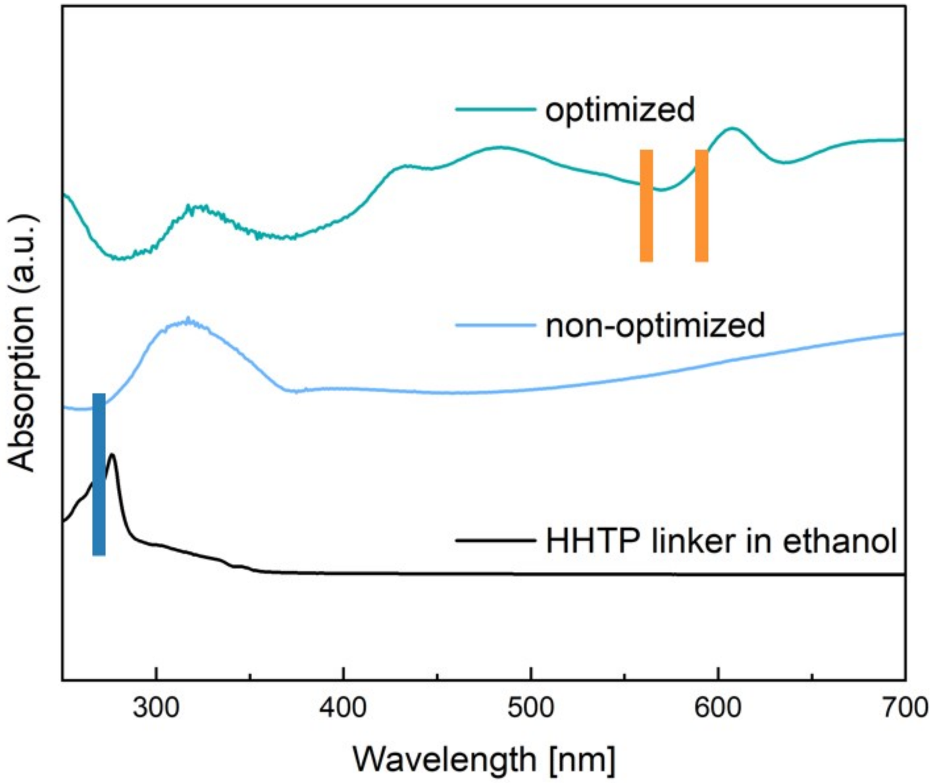

Figure S2. Experimental UV-Vis absorption spectra of HHTP chromophore (bottom), a $Cu_3(HHTP)_2$ SURMOF deposited using initial, non-optimized conditions (middle), and a SURMOF deposited using optimized conditions (top). The vertical lines show the results of DFT calculations (see Fig. 1, main document).

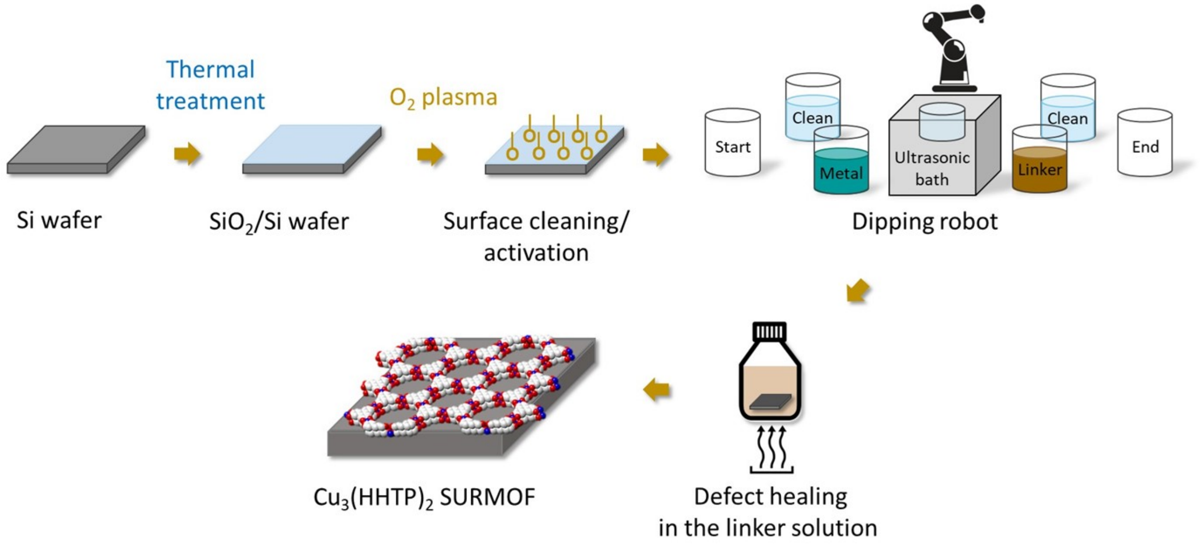

Figure S3. Layer-by-layer process for the preparation of Cu_3HHTP_2 SURMOFs.

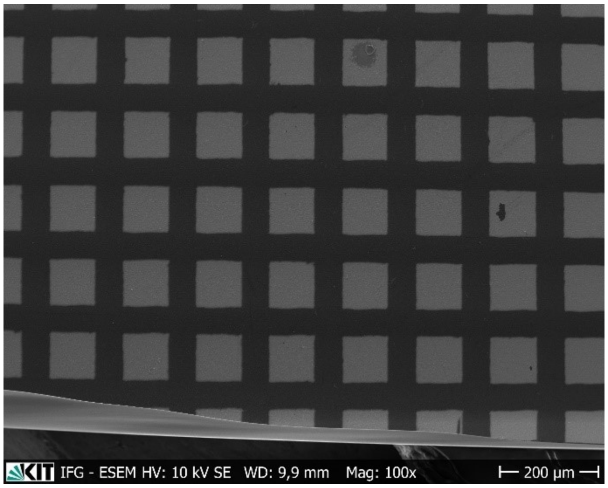

Figure S4. Gold contact pads deposited via a shadow mask (100 µm × 100 µm dimensions and spaced 100 µm apart) on the top surface of the $Cu_3(HHTP)_2$ film for the electrical conductivity measurement.

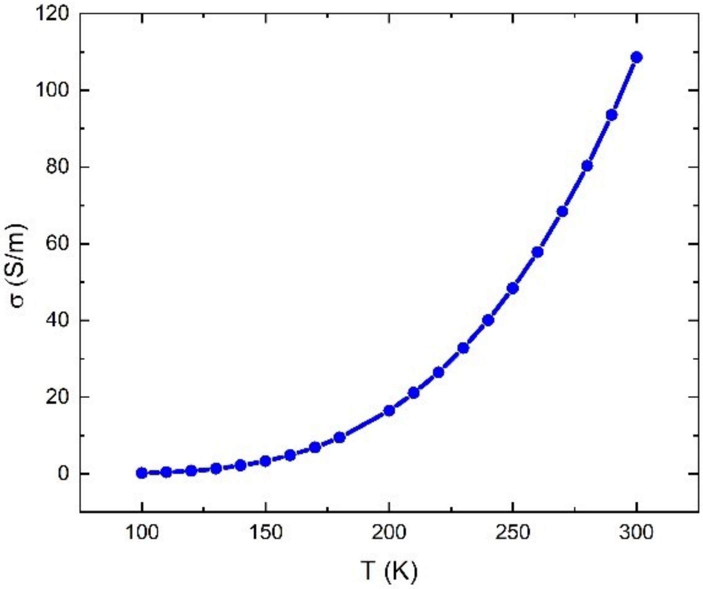

Figure S5. Temperature dependence of the electrical conductivity measured for the 100 µm contact spacing. (A corresponding measurement with an electrode spacing of 15 µm was also performed and revealed a conductivity of 113.5 S/m, only slightly larger than the 100 µm value.)

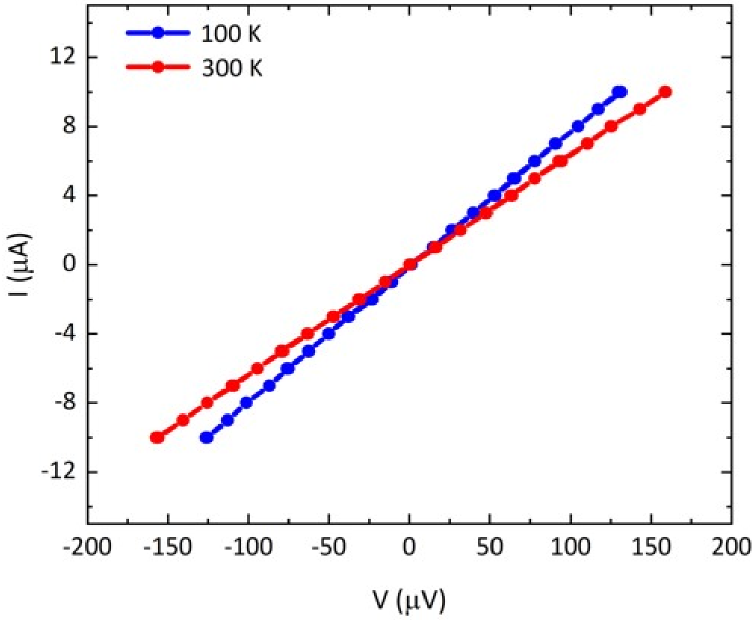

Figure S6. Linear IV characteristics of device with 100 nm contact separation showing linear I(V) indicative of a metallic contact between gold pads and the MOF film. The respective measurement temperature is indicated in the figure.

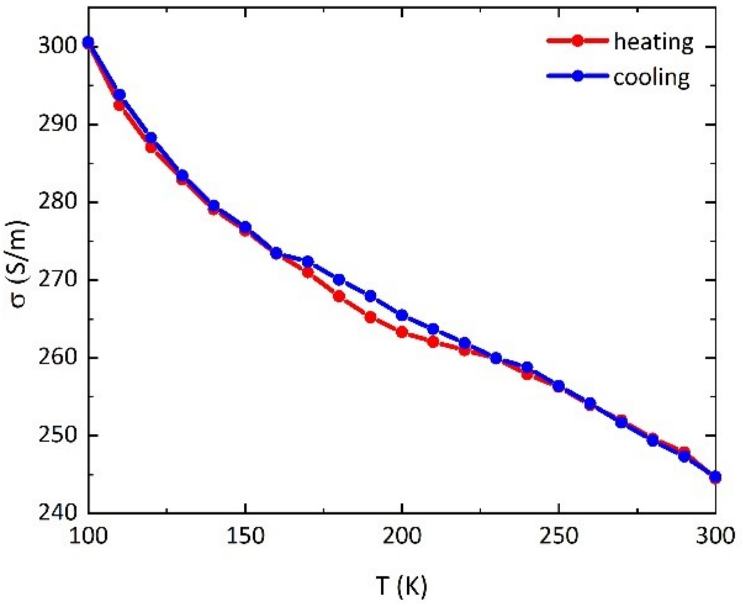

Figure S7. Electrical conductivity measured in a device with 100 nm contact separation in the temperature range of 100 K to 300 K under heating (red) and cooling (blue) of the sample.

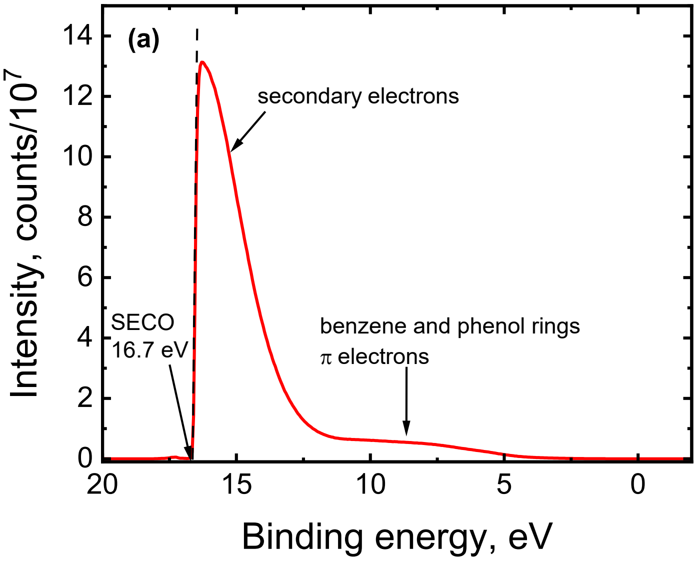
(a)
Intensity, counts/10^7
14
12
10
8
6
4
2
0
20
15
10
5
0
Binding energy, eV
secondary electrons
SECO
16.7 eV
benzene and phenol rings
π electrons

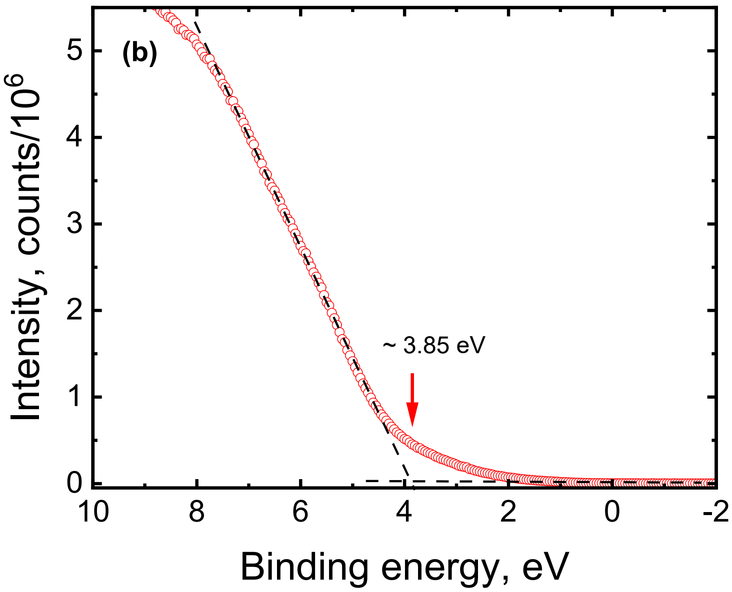
(b)
Intensity, counts/10^6
5
4
3
2
1
0
10
8
6
4
2
0
-2
Binding energy, eV
~ 3.85 eV

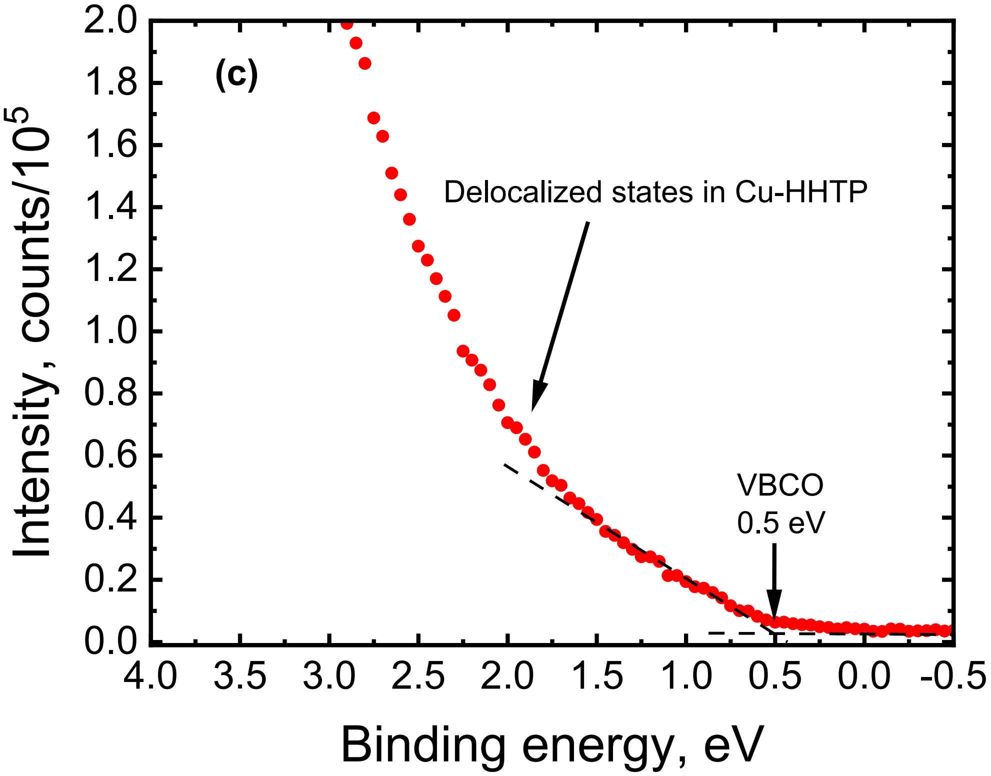

Figure S8. He I UPS data of a $Cu_3(HHTP)_2$ SURMOF on SiO_2/Si at 295 K. The data were acquired with a Scienta R4000 analyzer with a pass energy of 2 eV using a procedure described by Whitten.[20] The angles between the sample plane and entrance to the energy analyzer and He I lamp were ca. 90° and 45°, respectively. a) Photoelectron signal plotted as a function of binding energy (zero corresponding to the position of the Fermi level) with the tangent line to determine the value of the second electron cutoff (SECO) included. b) Photoelectron signal as a function of binding energy, expanded in the region near the Fermi level with the tangent lines to determine the HOMO of benzene/phenol rings. c) Further expansion of the region near the vacuum level cutoff (VBCO).

Side view of the CuHHTP SURMOFs

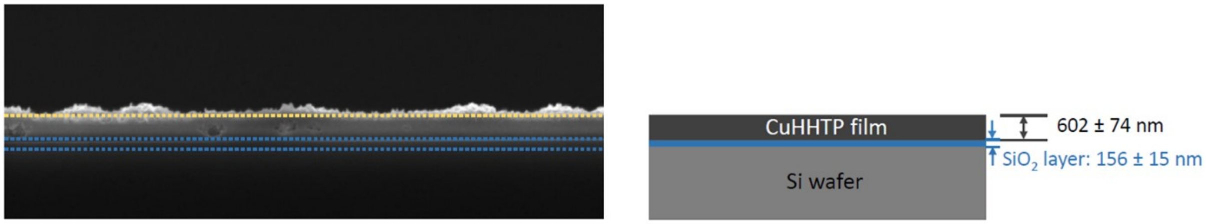

Figure S9. SEM micrograph recorded of an exemplary cross-section for $Cu_3(HHTP)_2$ SURMOFs grown on SiO_2/Si substrate showing the average thickness of 602nm ±74nm.

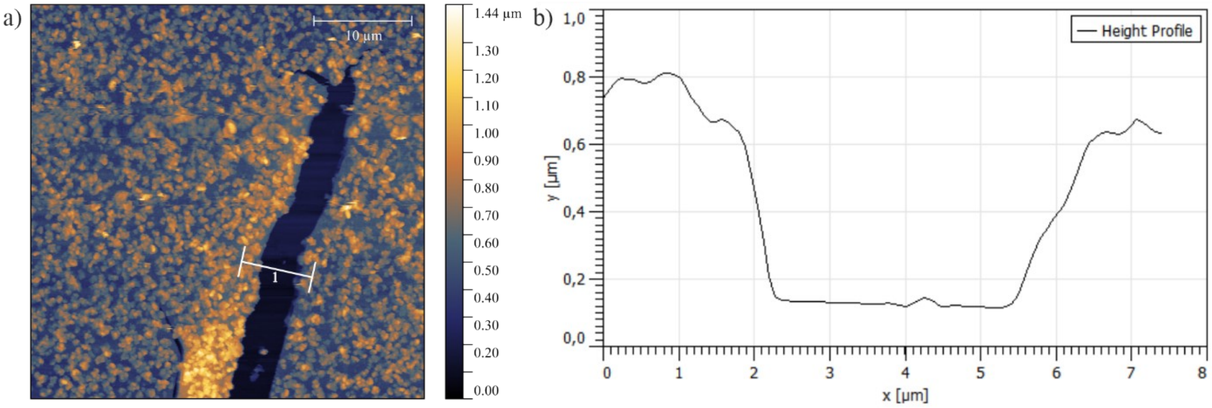

Figure S10. AFM image of cut in a $Cu_3(HHTP)_2$ SURMOFs grown on a glass substrate. The line cut, measured in the marked area and averaged over a width of 3 µm shows an average film thickness of 648 ± 67 nm.

References

[1] S. M. Moosavi, A. Chidambaram, L. Talirz, M. Haranczyk, K. C. Stylianou, B. Smit, *Nature Communications* **2019**, *10*, 539.

[2] R. W. Day, D. K. Bediako, M. Rezaee, L. R. Parent, G. Skorupskii, M. Q. Arguilla, C. H. Hendon, I. Stassen, N. C. Gianneschi, P. Kim, M. Dincă, *ACS Central Science* **2019**, *5*, 1959-1964.

[3] M. Hmadeh, Z. Lu, Z. Liu, F. Gándara, H. Furukawa, S. Wan, V. Augustyn, R. Chang, L. Liao, F. Zhou, E. Perre, V. Ozolins, K. Suenaga, X. Duan, B. Dunn, Y. Yamamto, O. Terasaki, O. M. Yaghi, *Chemistry of Materials* **2012**, *24*, 3511-3513.

[4] X. Song, X. Wang, Y. Li, C. Zheng, B. Zhang, C.-a. Di, F. Li, C. Jin, W. Mi, L. Chen, W. Hu, *Angewandte Chemie International Edition* **2020**, *59*, 1118-1123.

[5] W. Zhao, T. Chen, W. Wang, S. Bi, M. Jiang, K. Y. Zhang, S. Liu, W. Huang, Q. Zhao, *Advanced Materials Interfaces* **2021**, *8*, 2100308.

[6] Y. Liu, Y. Wei, M. Liu, Y. Bai, X. Wang, S. Shang, J. Chen, Y. Liu, *Angewandte Chemie International Edition* **2021**, *60*, 2887-2891.

[7] B. Hoppe, K. D. J. Hindricks, D. P. Warwas, H. A. Schulze, A. Mohmeyer, T. J. Pinkvos, S. Zailskas, M. R. Krey, C. Belke, S. König, M. Fröba, R. J. Haug, P. Behrens, *CrystEngComm* **2018**, *20*, 6458-6471.

[8] M.-S. Yao, X.-J. Lv, Z.-H. Fu, W.-H. Li, W.-H. Deng, G.-D. Wu, G. Xu, *Angewandte Chemie International Edition* **2017**, *56*, 16510-16514.

[9] M. de Lourdes Gonzalez-Juarez, C. Morales, J. I. Flege, E. Flores, M. Martin-Gonzalez, I. Nandhakumar, D. Bradshaw, *ACS Applied Materials & Interfaces* **2022**, *14*, 12404-12411.

[10] V. Rubio-Giménez, M. Galbiati, J. Castells-Gil, N. Almora-Barrios, J. Navarro-Sánchez, G. Escorcia-Ariza, M. Mattera, T. Arnold, J. Rawle, S. Tatay, E. Coronado, C. Martí-Gastaldo, *Advanced Materials* **2018**, *30*, 1704291.

[11] K. M. Snook, L. B. Zasada, D. Chehada, D. J. Xiao, *Chemical Science* **2022**, *13*, 10472-10478.

[12] K. W. Nam, S. S. Park, R. dos Reis, V. P. Dravid, H. Kim, C. A. Mirkin, J. F. Stoddart, *Nature Communications* **2019**, *10*, 4948.

[13] M. Ko, A. Aykanat, M. K. Smith, K. A. Mirica, in *Sensors, Vol. 17*, **2017**.

[14] J. M. Wrogemann, M. J. Lüther, P. Bärmann, M. Lounasvuori, A. Javed, M. Tiemann, R. Golnak, J. Xiao, T. Petit, T. Placke, M. Winter, *Angewandte Chemie International Edition* **2023**, *62*, e202303111.

[15] Y. Misumi, A. Yamaguchi, Z. Zhang, T. Matsushita, N. Wada, M. Tsuchiizu, K. Awaga, *Journal of the American Chemical Society* **2020**, *142*, 16513-16517.

[16] M. K. Smith, K. E. Jensen, P. A. Pivak, K. A. Mirica, *Chemistry of Materials* **2016**, *28*, 5264-5268.

[17] J. W. Gittins, C. J. Balhatchet, Y. Chen, C. Liu, D. G. Madden, S. Britto, M. J. Golomb, A. Walsh, D. Fairen-Jimenez, S. E. Dutton, A. C. Forse, *Journal of Materials Chemistry A* **2021**, *9*, 16006-16015.

[18] W.-H. Li, K. Ding, H.-R. Tian, M.-S. Yao, B. Nath, W.-H. Deng, Y. Wang, G. Xu, *Advanced Functional Materials* **2017**, *27*, 1702067.

[19] A. Dong, Z. Mu, X. Meng, S. Li, J. Li, L. Dai, J. Lv, P. Li, B. Wang, *Chemical Engineering Journal* **2022**, *444*, 136574.

[20] J. E. Whitten, *Applied Surface Science Advances* **2023**, *13* 100384.